Investigation of photocatalytic activity of nickel-doped manganese aluminum ferrite nanoparticles for rhodamine b degradation under visible light

Muhammad Yasar (mayoyasar@gmail.com)
Bahauddin Zakariya University

Research Article

Keywords: Nickel-Doping, Spinel Ferrite, Sol-Gel Synthesis, Visible Light Photocatalysis, Rhodamine B Degradation, Wastewater Treatment

Posted Date: December 13th, 2023

DOI: https://doi.org/10.21203/rs.3.rs-3736958/v1

Additional Declarations: No competing interests reported.

Abstract

Nickel-doped manganese aluminum ferrite $Ni_XMn_{1-X}Al_{0.5}Fe_{1.5}O_4$ (X = 0,0.3) nanoparticles were synthesized via the Sol-gel method. XRD showed the spinel ferrite structure with average crystallite sizes of 30.66 to 39.69 nm. FTIR confirmed metal-oxygen bonds. SEM revealed the surface morphology and particle sizes of 75–95 nm. EDX confirmed the elemental composition. BET analysis determined the surface area of 13.43 m^2/g for undoped and 28.38 m^2/g for Ni-doped ferrite. The band gap decreases from 2.4 to 2.2 by doping nickel. Achieving 98.96% degradation of 10 mg/L Rhodamine B within 120 min under visible light irradiation was accomplished using a catalyst dose of 0.1 g/L at pH 7 and 20°C with a light intensity of 100 W. The photodegradation kinetics followed a first-order reaction. Hydroxyl radicals were identified as the major reactive species responsible for dye degradation. The nickel-doped ferrite nanoparticles exhibited efficient and stable photocatalytic performance for Rhodamine B removal from wastewater under visible light. Photocatalytic performance for Rhodamine B removal from wastewater under visible light.

1 Introduction

Rhodamine B is a synthetic dye that is widely used in a variety of applications, including textiles, food, and cosmetics. It is also used as a tracer dye in water pollution studies. However, rhodamine B is a toxic and persistent organic pollutant that can have several negative effects on the environment [1, 2]. Rhodamine B is toxic to aquatic organisms and can bioaccumulate in their bodies. It is a persistent organic pollutant that can remain in the environment for long periods, posing a risk to aquatic life and humans. Rhodamine B is toxic to humans and can cause skin irritation, eye irritation, respiratory problems, digestive problems, and cancer [3, 4]. Rhodamine B is resistant to biodegradation due to its stable structure, so it persists in natural environments and wastewater systems after use. Conventional biological and chemical treatment methods have had limited success in removing Rhodamine B from water [5]. Hence, there is a need for innovative treatment approaches to effectively decolorize and degrade this recalcitrant dye.

Semiconductor photocatalysis has emerged as a promising advanced oxidation process for treating organic pollutants in wastewater. Under light irradiation, photogenerated electrons and holes in the semiconductor can react with water and oxygen to produce highly reactive hydroxyl and superoxide radicals. These radicals can non-selectively oxidize dye molecules adsorbed on the photocatalyst surface [6, 7]. A wide range of semiconductor photocatalysts like TiO_2, ZnO, WO_3, and ferrites have been explored for dye degradation. Among ferrites, manganese aluminum ferrite possesses attractive properties like visible light absorption, corrosion resistance, low cost, and environmental compatibility [8, 9]. However, pristine MAF suffers from fast recombination of photogenerated charge carriers which limits its activity.

Spinel ferrites have the general formula MFe_2O_4 where M is a divalent metal cation like Mn, Ni, Cu, Mg, etc. They possess an inverse spinel structure with oxygen forming a FCC closed packing, and metal cations occupying interstitial tetrahedral and octahedral sites. Spinel ferrites exhibit unique electric, magnetic, and optical properties that make them useful for a wide range of applications including photocatalysis. Their properties can be tuned by varying the composition and preparation conditions. Among ferrites, manganese aluminum ferrite possesses attractive properties like visible light absorption, corrosion resistance, low cost, and environmental compatibility [10–12]. However, pristine manganese aluminum ferrite suffers from fast recombination of photogenerated charge carriers which limits its activity.

Doping with transition metal ions is an effective strategy to improve the photocatalytic performance of metal oxides [9]. Nickel is a promising dopant for enhancing the photo response of ferrite photocatalysts. The incorporation of Ni^{2+} introduces additional energy levels in the bandgap of manganese aluminum ferrite, which can promote charge carrier separation and extend light absorption to the visible region [13]. However, the photocatalytic efficiency is strongly dependent on the nickel doping concentration, as it influences surface area, crystallinity, band structure, and other material properties [14]. There have been very few systematic studies on identifying the optimal Ni doping level for maximizing the photodegradation of Rhodamine B by photocatalysts.

This work aims to synthesize nickel-doped manganese aluminum ferrite with different dopant concentrations via the sol-gel combustion technique and evaluate their photocatalytic activity for decolorizing Rhodamine B under visible light. The synthesized photocatalysts will be thoroughly characterized and tested for degradation of Rhodamine B in a batch photoreactor under varying conditions. Kinetics of the photodegradation reaction will also be investigated. The insights from this work can aid in the rational design of efficient nickel-doped ferrite photocatalysts for the treatment of wastewater containing dye pollutants.

2. Materials and Methods

2.1 Materials

All the necessary chemicals, such as nickel nitrate hexahydrate, manganese nitrate tetrahydrate, aluminum nitrate nonahydrate, iron nitrate hexahydrate, sodium hydroxide, hydrochloric acid, and Rhodamine B dye, were carefully selected from the reputable supplier. These chemicals were specifically chosen for their high quality and purity, as they were of analytical grade and required no further purification. To ensure the accuracy of our experiments, distilled water was exclusively used for the preparation of solutions.

2.2 Synthesis of Nickle-doped manganese aluminum ferrite nanoparticles

The Sol-gel technique has been employed to synthesize the impressive $Ni_XMn_{1-X}Al_{0.5}Fe_{1.5}O_4$ (X = 0,0.3) nanoparticles. To achieve the desired stoichiometric composition, it is crucial to carefully measure precise quantities of nickel nitrate, manganese nitrate, aluminum nitrate, and iron nitrate and combine them in a beaker. Dissolve the metal nitrates in distilled water and stir well to get a clear solution. Add citric acid to this solution in a 1:1 molar ratio concerning the total moles of metal nitrates. Stir vigorously until a transparent solution is obtained. Adjust the pH of the solution between 7–8 using ammonia solution. To make a very viscous gel, heat the solution at 70–80°C with constant stirring. To acquire the fluffy power, dry the gel at 130°C to eliminate superfluous solvents. Calcinate the powder for 3 hours at 750°C. It cools down naturally to room temperature. Grind the calcined powder again to get the final product $Ni_XMn_{1-X}Al_{0.5}Fe_{1.5}O_4$ nanopowder.

2.2 Characterization of Nanoparticles

The synthesized $Ni_XMn_{1-X}Al_{0.5}Fe_{1.5}O_4$ (X = 0,0.3) nanoparticles were characterized by XRD used Crystal structure and phase purity, FTIR was used for Functional groups on the surface, SEM was used for Surface morphology and size, EDX was used for elemental composition, BET used for Specific surface area and Electrical resistivity used material resists the flow of electric current.

2.3 Photocatalytic Activity Experiments

The nanoparticles of ferrite were tested for their photocatalytic activity by observing the degradation of Rhodamine B dye under exposure to visible light. A halogen lamp of 100 W was utilized as the visible source of light. In a standard test, a glass beaker was filled with an aqueous solution containing Rhodamine B (10 mg/L) and the catalyst (100 mg/L). The mixture was stirred in the dark for 60 minutes before irradiation to achieve adsorption-desorption equilibrium. Samples were collected at specific time intervals, centrifuged to separate particles, and then examined with a UV-vis spectrophotometer. Various operational parameters such as pH of the solution, temperature of the reaction, initial concentration of Rhodamine B, dosage of the catalyst, addition of hydrogen peroxide, and intensity of light were studied. The catalyst's reusability was also assessed over multiple cycles. To identify the active species, trapping tests were conducted using scavengers for hydroxyl radicals (•OH), holes (h+), and superoxide radicals (O2−•). The efficiency of degradation was calculated using a specific mathematical formula.

$$\mathrm{Degradation}\,(\%) = \frac{\mathrm{C_0} - \mathrm{C_t}}{\mathrm{C_0}} \times 100$$

1

The symbol C_0 indicates the initial concentration, whereas C_t represents the concentration remaining at a certain time, denoted as t.

3. Results and Discussion

3.1 XRD Analysis

The X-ray diffraction (XRD) patterns of nickel-doped manganese aluminum ferrite $Ni_XMn_{1-X}Al_{0.5}Fe_{1.5}O_4$ (X = 0,0.3) nanoparticles prepared with X = 0 and 0.3 showed distinct diffraction peaks at 2θ = 18.5°, 29.8°, 35.1°, 42.7°, 52.9°, and 62.5°, which are attributed to the (111), (220), (311), (400), (422), and (440) planes of the cubic spinel ferrite structure. The absence of impurity peaks indicates the high phase purity of the synthesized materials. The average crystallite size, calculated using the Scherrer equation, was 30 and 39 nm for $Ni_{0.3}Mn_{0.7}Al_{0.5}Fe_{1.5}O_4$ and $Mn_1Al_{0.5}Fe_{1.5}O_4$, respectively.

Table 1
The XRD Structural parameters of the synthesized MixMn1−xAl0.5Fe1.5O4 (X = 0,0.3) ferrite

Parameters	**$Mn_1Al_{0.5}Fe_{1.5}O_4$**	**$Ni_{0.3}Mn_{0.7}Al_{0.5}Fe_{1.5}O_4$**
FWHM	0.1987	0.2576
D-Spacing	2.5546	2.5267
Lattice constant (Å)	8.4726	8.3801
Cell Volume (Å)3	608.194	588.503
Hoping length La (Å)	3.668	3.628
Hoping length Lb (Å)	2.995	2.962
Crystalline size (nm)	39.79	30.66
X-Ray Density (g/cm3)	2.77E-18	3.67E-18
Dislocation density (g/cm3)	0.000631	0.001063
Lattice strain	0.0157	0.0206
Micro-Strain (lines/m-4)	0.0473	0.0613

The lattice parameter was determined to be 8.47 and 8.38 nm for $Mn_1Al_{0.5}Fe_{1.5}O_4$ and $Ni_{0.3}Mn_{0.7}Al_{0.5}Fe_{1.5}O_4$, respectively. As the Ni content increased the ferrite peaks became slightly broader and less intense, suggesting a decrease in crystallinity due to the substitution of Ni^{2+} ions in the ferrite lattice. Based on the data in Table 1, it appears that the following parameters decrease with nickel doping: lattice constant, cell volume, hoping length La, hoping length Lb, crystalline size, and X-ray density. There are a few possible explanations for these observations. One possibility is that the nickel ions are smaller than the manganese ions they are replacing, which would lead to a decrease in the lattice constant and cell volume. Additionally, the nickel ions may be causing distortions in the crystal lattice, which would also lead to a decrease in the hoping length La and hoping length Lb. Finally, the nickel ions may be causing the formation of smaller crystals, which would lead to a decrease in the crystalline size. Another possibility is that the nickel ions are causing an increase in the dislocation density, which would lead to an increase in the micro-strain. The dislocation density is a measure of the number of dislocations in a material, and dislocations are imperfections in the crystal lattice that can cause strain.

3.2 FTIR Analysis

FTIR spectroscopy provides valuable insights into the structural parameters of materials. Ferrites exhibit two distinct M-O vibration frequencies: the first (550 – 443 cm ^{1}) corresponds to octahedral (B-site) M-O stretching vibrations, while the second (527 – 523 cm ^{1}) arises from tetrahedral (A-site) M-O stretching vibrations can be seen in Fig. 2. The presence of a band at 654 cm ^{1} indicates Al–O-Al bending vibrations. New bands at 892 cm ^{1} confirm Fe-OH bond formation. Peaks at 1063 and 1057 cm ^{1} correspond to Al–OH bending and stretching vibrations. The residual FeO-OH group was observed at 1177 and 1178 cm ^{1} (OH-deformation vibrations). The faint peak at 1397 and 1395 cm ^{1} is due to asymmetric NO^{3} stretching vibrations in residual nitrate groups. With the increasing Ni concentration, both v1 and v2 bands shifted, confirming the spinel structure. The observed peak shifts are attributed to changes in cation occupancy in tetrahedral (A) and octahedral (B) sites. The decrease in bond lengths leads to the observed increase in absorption frequency.

3.3 Scanning Electron Microscopy

The SEM micrograph shows the morphology of the $Ni_XMn_{1-X}Al_{0.5}Fe_{1.5}O_4$ (X = 0). The grains are arranged in a variety of shapes and sizes, but most are roughly equiaxed. The grains are separated by grain boundaries. The SEM image also shows that the $Ni_XMn_{1-X}Al_{0.5}Fe_{1.5}O4$ (X = 0.3) particles are packed closely together. This is likely to be due to the high packing density of the powder. The SEM image shows that doping of nickel $Ni_XMn_{1-X}Al_{0.5}Fe_{1.5}O_4$ (X = 0,0.3) can have a significant impact on the grain size of the material. This decrease in grain size 90 – 75 nm is due to the disruption of the crystal structure by the nickel doping (J image software used to determine grain size). The decrease in grain size is beneficial for several reasons, including improved strength, toughness, corrosion resistance, and electrical conductivity.

3.4 EDX Analysis

EDX spectra are used to identify and quantify the elemental composition of a material. In this case, the EDX spectra of the ferrite nanoparticles confirmed that the synthesis process was successful and that the nanoparticles have the expected stoichiometric composition. This means that the nanoparticles contain the correct proportions of each element. The absence of impurity elements in the spectra indicates that the synthesis process was clean and that there are no unexpected elements present in the nanoparticles can be seen in Fig. 4. This is important because impurities can affect the properties of the nanoparticles. Energy-dispersive X-ray spectroscopy (EDX) analysis confirms the presence of Al, Ni, Mn, Fe, and O elements in the synthesized nanoparticles. The intensity of each signal corresponds to the relative abundance of the respective element in the nanoparticles.

3.5 BET Analysis

The Nitrogen adsorption-desorption isotherm technique was used to determine the specific surface area, pore size distribution, and pore volume of the $Ni_XMn_{1-X}Al_{0.5}Fe_{1.5}O_4$ (X = 0,0.3) catalysts. The results are shown in Table 2. As can be seen, the BET surface area of the sample increased from 13.43 m^2/g to 28.8

$m^{2/}g$ as the nickel doping concentration increased. This is a significant increase in surface area, and it can be attributed to the formation of new nickel-containing active sites on the surface of the catalyst. Additionally, the average pore size increased from 19.35 Å to 35.6 Å as the nickel doping concentration increased. This increase in pore size is also beneficial for the catalytic activity of the material, as it allows larger molecules to access the active sites. The positive correlation between the doping concentration of nickel and the surface area and pore size is clearly shown in Fig. 5. As the nickel doping concentration increases, the surface area and pore size both increase. This is because nickel atoms can act as nucleation sites for the formation of new pores.

Table .2: Adsorption Description results of Nitrogen of the $Ni_XMn_{1-X}Al_{0.5}Fe_{1.5}O_4$ (X = 0,0.3)

Sample	Bet Surface Area ($m^2\ g^{-1}$)	Total pore volume (cm^3g^{-1})	Average pore radius (Å)
$Mn_1Al_{0.5}Fe_{1.5}O_4$	13.43	0.456	19.35
$Ni_{0.3}Mn_{0.7}Al_{0.5}Fe_{1.5}O_4$	28.38	1.675	35.6

2.6 Electrical Resistivity

The resistance of $Ni_XMn_{1-X}Al_{0.5}Fe_{1.5}O_4$ (X = 0,0.3) spinel ferrites as a function of temperature. The resistance of both samples increases as the temperature increases. The graph shows that the electrical resistivity of $Ni_{0.3}Mn_{0.7}Al_{0.5}Fe_{1.5}O_4$ is lower than that of $Mn_1Al_{0.5}Fe_{1.5}O_4$ at all temperatures. This is because $Ni_{0.3}Mn_{0.7}Al_{0.5}Fe_{1.5}O_4$ is a mixed metal oxide, which means that it contains both metal and oxide ions. Metal ions have free electrons that can conduct electricity, while oxide ions do not. Therefore, the presence of nickel ions in $Ni_{0.3}Mn_{0.7}Al_{0.5}Fe_{1.5}O_4$ reduces its electrical resistivity. Overall, the electrical resistivity of the materials increases with temperature. This is due to the increased vibration of atoms and the formation of defects at higher temperatures.

3.7 Photodegradation Experiments

3.7.1 Doping effect on photodegradation

The fact that photolysis observed no degradation suggests that the photodegradation observed in the presence of the Ni-doped catalyst is due to a catalytic effect of the catalyst, rather than direct photolysis of the pollutant in illustrated Fig. 7 **(a).** This is further supported by the observation that the photodegradation efficiency is significantly higher for the Ni-doped catalyst (98.96%) than for the undoped catalyst (83%). Ni-doped catalyst improves photodegradation by absorbing more visible light, preventing electron-hole recombination, and increasing the number of active sites [15].

3.7.2 Effect of pH

The photodegradation of rhodamine B was evaluated at pH 3 to 11 and was found to be 99.80–83.23%, respectively in illustrated Fig. 7 **(b).** This is because the protonated form of rhodamine B is more susceptible to photodegradation. At low pH, rhodamine B is protonated, which increases its positive charge and makes it more reactive with hydroxyl radicals. At high pH, rhodamine B is deprotonated, which reduces its positive charge and makes it less reactive with hydroxyl radicals in addition, Rhodamine B aggregates at high pH, making them more difficult to photodegrade.

3.7.3 Effect of Dye Concentration

The degradation of rhodamine B decreased from 99.61% at 5 ppm to 62% at 50 ppm. This is a significant decrease, and the dye concentration has a strong influence on the photodegradation rate illustrated in Fig. 7 **(c).** The decrease in photodegradation of rhodamine B with increasing dye concentration can be attributed to *Limited active sites*: Competition for active sites between rhodamine B molecules and hydroxyl radicals decreases the number of rhodamine B molecules that are degraded. *Self-shielding*: Dye molecules absorb photons of light before they reach the photocatalyst surface, preventing photocatalyst activation and hydroxyl radical generation. *Reaction intermediates*: The formation of reaction intermediates competes with rhodamine B molecules for active sites and hydroxyl radicals, decreasing the degradation efficiency[16].

3.7.4 Effect of Catalyst Dosage

The photodegradation of rhodamine B increased from 98.96–99.8% as the catalyst dosage was increased from 100 mg to 250 mg but decreased to 76% when the dosage was increased to 300 mg. The photodegradation of rhodamine B increased as the catalyst dosage increased up to an optimal value, and then decreased beyond that value can be seen in Fig. 7 **(d).** This is because increasing the catalyst dosage increases the number of active sites available to generate reactive oxygen species (ROS) which degrade the dye molecules. However, too much catalyst can lead to self-shading, where the catalyst particles block each other from accessing light, and agglomeration, where the catalyst particles clump together and reduce their surface area [17].

3.7.5 Effect of Temperature

The photodegradation of rhodamine B increased from 98.96% at 20℃ to 99.07% at 40 ℃ and 99.80% at 60 ℃ illustrated in Fig. 8 **(a).** This increase in photodegradation with increasing temperature can be attributed to the following factors. At higher temperatures, the mobility of rhodamine B molecules increases, making it easier for them to encounter the photocatalyst and absorb photons of light. Additionally, the adsorption capacity of the photocatalyst increases at higher temperatures, leading to more rhodamine B molecules being available for photodegradation [18]. Finally, the generation of hydroxyl radicals, which are the primary reactive species responsible for the photodegradation of rhodamine B, also increases at higher temperatures.

3.7.6 Effect of Light Intensity

The degradation efficiency of RhB under 100 W, 200 W, and sunlight illumination was 98.96%, 99.8%, and 99.8%, respectively illustrated in Fig. 8 **(b).** The photodegradation rate of Rhodamine B is directly proportional to light intensity. This is because higher light intensity generates more electron-hole pairs on the photocatalyst surface, which enhances the production of reactive oxygen species (ROS), such as hydroxyl radicals ($OH^{\cdot}$), superoxide radicals ($O_2^{\cdot}$), and hydrogen peroxide (H_2O_2). These ROS are the primary oxidants responsible for the degradation of Rhodamine B. Sunlight is the most abundant and renewable source of light energy for photocatalytic degradation, as it contains both UV and visible light, which can excite a wide range of photocatalysts.

3.7.7 Effect of H_2O_2 Addition

Adding hydrogen peroxide (H_2O_2) increased the degradation of rhodamine B dye up to a concentration of 6 mM H_2O_2. Degradation increased from 83.96–98.61% as the H_2O_2 concentration was raised from 0 to 6 mM. However, at 8 mM H_2O_2, degradation decreased to 77.61% illustrated in Fig. 8 **(c).** The increase in degradation is attributed to higher production of hydroxyl radicals (HO•) at higher H_2O_2 levels, which degrade the dye. The subsequent drop in degradation at 8 mM H_2O_2 is due to (a) scavenging of HO• by excess H_2O_2, (b) formation of less reactive per hydroxyl radicals (HO_2•) from HO• at high H_2O_2 levels, and (c) inhibition of the Fenton reaction by high H_2O_2 competing with dye for HO• and complexing the catalyst [19].

3.7.8 Scavenger Analysis

To pinpoint the primary reactive species, the impacts of scavengers such as benzoquinone (a scavenger for O2−•), tert-butyl alcohol (a scavenger for OH•), and ethylenediaminetetraacetic acid (a scavenger for h+) were investigated [20]. It was found that hydroxyl radicals are the key species driving the degradation of Rhodamine B (degraded 48% with TBA, a scavenger of hydroxyl radicals, compared to 98.96% with no scavenger) illustrated in Fig. 8 **(d).** Scavenging experiments with benzoquinone (BQ) and ethylenediaminetetraacetic acid (EDTA), scavengers of superoxide radicals ($O_2^{-\cdot}$) and metal ions, respectively, have little effect on the degradation of Rhodamine B (95% and 92% degradation, respectively).

3.7.9 Photodegradation Mechanism

A potential mechanism for the photodegradation of Rhodamine B over the ferrite photocatalyst was suggested based on the trapping experiments. When exposed to visible light, electron-hole pairs are formed. These holes oxidize water that is adsorbed on the surface, resulting in the creation of highly reactive OH• radicals. Electrons are trapped by surface defects or react with dissolved O_2 to give O_2– radicals. The Rhodamine B molecules are then degraded by these reactive species through oxidation, decomposition, and mineralization reactions. When ferrite undergoes irradiation, the process of electron excitation from the valence band to the conduction band occurs[21]. This generates holes that lead to the production of hydroxyl radicals, as described below:

Step 1

Generation of electron-hole pairs

$$\mathrm{Ni_{0.3}Mn_{0.7}Al_{0.5}Fe_{1.5}O_4} + hv \rightarrow \mathrm{Ni_{0.3}Mn_{0.7}Al_{0.5}Fe_{1.5}}O_4^* + \mathrm{e}^- + \mathrm{h}^+ \,(2)$$

where: $Ni_{0.3}Mn_{0.7}Al_{0.5}Fe_{1.5}O_4$is the ferrite photocatalyst, hv is a photon of visible light, $\mathrm{Ni_{0.3}Mn_{0.7}Al_{0.5}Fe_{1.5}}O_4^*$is the excited ferrite photocatalyst, e is an electron and h is a hole.

Step 2

Oxidation of surface adsorbed water

$$h^+ + H_2O \rightarrow OH^* + H^+ \,(3)$$

where: OH^* is a hydroxyl radical

Step 3

Trapping of electrons

$$e^- + O_2 \rightarrow O_2^{*-} \,(4)$$

where: O_2^{*-} is a superoxide radical

Step 4

Degradation of Rhodamine B

$$RhB + OH^* \rightarrow intermediates \rightarrow CO_2 + H_2O + Otherinorganicproducts$$

5

Or

$$RhB + O_2^{*-} \rightarrow intermediates \rightarrow CO_2 + H_2O + Otherinorganicproducts \,(6)$$

The overall reaction for the photodegradation of Rhodamine B can be written as:

$$RhB + \mathrm{Ferrite} + hv \rightarrow CO_2 + H_2O + Otherinorganicproducts + Ferrite \,(7)$$

The dye photodegradation by visible light irradiation is an effective and environmentally friendly technique that produces only CO_2 and H_2O as end products [22].

3.7.10 Optical Properties

The Tauc equation, which is used to determine the band gap of both direct and indirect semiconductors, can be expressed as follows:

$$\alpha \mathrm{hv} = \mathrm{A}\left(\mathrm{hv} - \mathrm{Eg}\right)^{n}\,(8)$$

In this context: α represents the absorption coefficient at a given photon energy hv, A is a constant value, Eg refers to the band gap, and n is a constant that varies based on the specific type of semiconductor. Nickel (Ni) doping in $Ni_XMn_{1-X}Al_{0.5}Fe_{1.5}O_4$ can decrease the band gap from 2.4 to 2.2 eV can be seen in Fig. 9. Nickel doping enhances photodegradation by introducing new energy levels within the band gap, leading to increased absorption of visible light and the generation of more electron-hole pairs. Additionally, Ni atoms act as electron traps, preventing recombination and extending the lifetimes of these charge carriers, further enhancing photocatalytic activity.

2.7.12 Kinetics

A kinetic study was undertaken to elucidate the reaction order of the decomposition of rhodamine B. The concentration of RhB was monitored over time. The concentration data was fitted to equations for first order and second-order reaction kinetics, given below:

First-order rate equation:

$$\ln\left(\frac{C_t}{C_0}\right)(9)$$

Second-order rate equation:

$$\frac{1}{C_t} = \frac{1}{C_0} + K_t\,(10)$$

In this context: C_t represents the concentration at a specific time ‘t’, C_0 denotes the initial concentration, ‘k’ is the rate constant, and ‘t’ is the time elapsed. The evaluation of the kinetic data indicates that the decomposition reaction aligns more accurately with first-order kinetics, as evidenced by a high R^2 value of 0.998 for the first-order plot shown in Fig. 10 **(a)**. The second-order plot Fig. 11 **(b)** gave a slightly lower R^2 value of 0.917. These results provide clear evidence that the decomposition of RhB at this concentration follows first-order kinetics. The reaction rate is dependent on the concentration of RhB, indicating a mechanism involving one molecule of dye reacting in the rate-determining step. This kinetic study elucidates the rate law and reveals insights into the reaction mechanism.

3.7.13 Comparison Study

Table 3 presents a comparison of various photocatalytic materials and their effectiveness in breaking down the Rhodamine B dye under the influence of visible or UV light. It compares the photocatalytic activity of different composite materials containing iron oxide with additions like ZnO, CuS, graphene oxide, etc. The key metric assessed is the removal efficiency of Rhodamine B dye after irradiation for different periods ranging from 90 minutes to 230 minutes. The catalyst dosage also varies from 0.1 g/L to 2.0 g/L for the different composites. Different light sources are tested - visible light vs UV light. The current study of nickel-doped manganese aluminum ferrite, which achieved 98.96% dye removal in 120 minutes using 0.1 g/L catalyst dosage - was one of the best results.

Table 3
Photocatalytic degradation of Rhodamine B results as compared to previous studies

Compositions	**Light source**	**Time (minutes)**	**Catalyst dosage(g/L)**	**Removal efficiency (%)**	**Ref.**
$CoNd_{0.05}Fe_{1.95}O_4$	Visible light	120	0.15	94.7	[23]
$NiFe_2O_4$	UV light	105	1.5	84	[24]
$NiFe_2O_4$@HAp-Sn2+	Visible light	230	0.65	84.4	[25]
$NiFe_2O_4$	Visible light	120	0.35	90	[26]
ZnFe@CuS	Visible light	90	1.5	93	[27]
$ZnFe_2O_4$/graphene oxide	Visible light	180	1.3	94	[28]
Zn-doped Fe_3O_4	UV light	90	2.0	97	[29]
$ZnFe_2O_4$-50%@ ZnO	Visible light	160	0.5	79	[5]
$Ni_{0.3}Mn_{0.7}Al_{0.5}Fe_{1.5}O_4$	Visible light	120	0.1	98.96	Current study

3.7.14 Catalyst Recyclability

The recyclability of the catalyst decreases with repeating cycles, with the degradation of rhodamine B decreasing from 98.96% in the first cycle to 95% in the fifth cycle shown in Fig. 11. This is likely due to several factors, including *Loss of catalyst*: The catalyst is lost during the degradation process, reducing the amount of catalyst available for the next cycle. *Deactivation of the catalyst*: The catalyst becomes deactivated over time, reducing its activity and ability to degrade rhodamine Fo*uling of the catalyst*: The catalyst is blocked by the reaction products or impurities, reducing its ability to degrade rhodamine B. The decrease in recyclability of the catalyst with repeating cycles is a common problem in catalysis.

Conclusion

The nickel-doped manganese aluminum ferrite nanoparticles synthesized in this work were thoroughly characterized. The broadening of the XRD peaks (311) indicates the FCC crystalline structure. XRD showed the spinel structure with average crystallite sizes of 30–39 nm. FTIR confirmed the metal-oxygen bonds. The SEM analysis indicated the particles are small and irregularly shaped and used to determine particle size range of 75–90 nm. BET analysis showed the surface area increased from 13.43 to 28.38 m^2/g after nickel doping. The electrical resistivity exhibits a positive temperature coefficient, indicating that resistance increases with increasing temperature. Under normal conditions, 99.8% degradation of 10 mg/L Rhodamine B was achieved in 120 min under 100 W visible light using 0.1 g/L catalyst at pH 7 and 20°C. First-order rate kinetics was followed. It was determined that hydroxyl radicals have a significant impact on the degradation of RhB. The nickel-doped ferrite demonstrated excellent photocatalytic activity, reusability for 5 cycles, and stability. This comprehensive study proves the potential of nickel-doped nanoparticles as efficient photocatalysts for dye removal using visible light.

Declarations

Conflict of Interests

The author declares that they have no financial or non-financial conflicts of interest that could influence the content or presentation of this work.

Author Contribution

Muhammad Yasar, the sole author of this paper, contributed comprehensively to all aspects of the research, writing, and preparation of this manuscript.

References

1. Yadav, A., Kang, S.-W. & Hunge, Y. (2021) Photocatalytic degradation of Rhodamine B using graphitic carbon nitride photocatalyst, *Journal of Materials Science: Materials in Electronics.* **32**, 15577-15585.
2. Zhang, M., Sun, X., Wang, C., Wang, Y., Tan, Z., Li, J. & Xi, B. (2022) Photocatalytic degradation of rhodamine B using Bi4O5Br2-doped ZSM-5, *Materials chemistry and physics.* **278**, 125697.
3. Waghchaure, R. H., Adole, V. A. & Jagdale, B. S. (2022) Photocatalytic degradation of methylene blue, rhodamine B, methyl orange and Eriochrome black T dyes by modified ZnO nanocatalysts: A concise review, *Inorganic Chemistry Communications*, 109764.
4. Kiran, K. K., Ramesh, D. & Shashanka, R. (2022) Photocatalytic Degradation of Rhodamine B Dye by Nanocomposites: A Review, *Applied Mechanics and Materials.* **908**, 119-129.
5. Nguyen, L. T., Vo, D.-V. N., Nguyen, L. T., Duong, A. T., Nguyen, H. Q., Chu, N. M., Nguyen, D. T. C. & Van Tran, T. (2022) Synthesis, characterization, and application of ZnFe2O4@ ZnO nanoparticles for photocatalytic degradation of Rhodamine B under visible-light illumination, *Environmental Technology & Innovation.* **25**, 102130.
6. Chankhanittha, T. & Nanan, S. (2021) Visible-light-driven photocatalytic degradation of ofloxacin (OFL) antibiotic and Rhodamine B (RhB) dye by solvothermally grown ZnO/Bi2MoO6 heterojunction,

Journal of Colloid and Interface Science. **582**, 412-427.

7. Ashiq, H., Nadeem, N., Mansha, A., Iqbal, J., Yaseen, M., Zahid, M. & Shahid, I. (2022) G-C3N4/Ag@ CoWO4: A novel sunlight active ternary nanocomposite for potential photocatalytic degradation of rhodamine B dye, *Journal of Physics and Chemistry of Solids.* **161**, 110437.
8. Sundararajan, M., Bonisha, B., Ubaidullah, M., Shaikh, S. M. F., Revathi, S., Thiripurasundari, D., Dhiwahar, A. T., Pandit, B., Dash, C. S. & Shahzad, M. (2022) Enhanced visible light photocatalytic degradation of rhodamine B using Ni1-xCaxFe2O4 (0≤ x≤ 0.5) nanoparticles: Performance, kinetics and mechanism, *Materials Research Bulletin.* **154**, 111911.
9. Dhiman, P., Rana, G., Kumar, A., Sharma, G., Vo, D.-V. N., AlGarni, T. S., Naushad, M. & ALOthman, Z. A. (2021) Nanostructured magnetic inverse spinel Ni–Zn ferrite as environmentally friendly visible light driven photo-degradation of levofloxacin, *Chemical Engineering Research and Design.* **175**, 85-101.
10. Jadhav, S. A., Somvanshi, S. B., Khedkar, M. V., Patade, S. R. & Jadhav, K. (2020) Magneto-structural and photocatalytic behavior of mixed Ni–Zn nano-spinel ferrites: visible light-enabled active photodegradation of rhodamine B, *Journal of Materials Science: Materials in Electronics.* **31**, 11352-11365.
11. Sharma, R. & Singhal, S. (2015) Photodegradation of textile dye using magnetically recyclable heterogeneous spinel ferrites, *Journal of Chemical Technology & Biotechnology.* **90**, 955-962.
12. Kirankumar, V. & Sumathi, S. (2020) A review on photodegradation of organic pollutants using spinel oxide, *Materials Today Chemistry.* **18**, 100355.
13. Cheng, Y., Zhang, S., Wang, Z., Wang, B., You, J., Guo, R. & Zhang, H. (2023) Review on spinel ferrites-based materials (MFe2O4) as photo-Fenton catalysts for degradation of organic pollutants, *Separation and Purification Technology*, 123971.
14. Dhiman, P., Rana, G., Alshgari, R. A., Kumar, A., Sharma, G., Naushad, M. & ALOthman, Z. A. (2023) Magnetic Ni–Zn ferrite anchored on g-C3N4 as nano-photocatalyst for efficient photo-degradation of doxycycline from water, *Environmental Research.* **216**, 114665.
15. Devi, K. N., Devi, S. A., Singh, W. J. & Singh, K. J. (2021) Nickel doped zinc oxide with improved photocatalytic activity for Malachite Green Dye degradation and parameters affecting the degradation, *Journal of Materials Science: Materials in Electronics.* **32**, 8733-8745.
16. Meena, P. L., Poswal, K., Surela, A. K. & Saini, J. K. (2023) Synthesis of graphitic carbon nitride/zinc oxide (g-C3N4/ZnO) hybrid nanostructures and investigation of the effect of ZnO on the photodegradation activity of g-C3N4 against the brilliant cresyl blue (BCB) dye under visible light irradiation, *Advanced Composites and Hybrid Materials.* **6**, 16.
17. Saeed, M., Muneer, M., Haq, A. u. & Akram, N. (2022) Photocatalysis: An effective tool for photodegradation of dyes—A review, *Environmental Science and Pollution Research*, 1-19.
18. Barapati, S., Mucherla, R., Gade, R. & Somaiah, P. V. (2022) Photodegradation of Rhodamine B and Crystal Violet using Al-doped Co–Mn nanoferrites and dielectric study, *Journal of Materials Science: Materials in Electronics.* **33**, 25139-25152.

19. Li, Z., Chen, Y., Guo, Y., Wang, Y., Guan, T., Bai, J., Hu, D., Li, H. & Du, J. (2022) Preparation of ultra-thin porous carbon nitride and its photocatalytic H2O2 production and photodegradation of RhB, *Applied Surface Science.* **598**, 153866.
20. Costa, L. N., Nobre, F. X., Lobo, A. O. & de Matos, J. M. E. (2021) Photodegradation of ciprofloxacin using Z-scheme TiO2/SnO2 nanostructures as a photocatalyst, *Environmental Nanotechnology, Monitoring & Management.* **16**, 100466.
21. Beshkar, F., Al-Nayili, A., Amiri, O., Salavati-Niasari, M. & Mousavi-Kamazani, M. (2022) Visible light-induced degradation of amoxicillin antibiotic by novel CuI/FePO4 pn heterojunction photocatalyst and photodegradation mechanism, *Journal of Alloys and Compounds.* **892**, 162176.
22. Khan, I., Saeed, K., Ali, N., Khan, I., Zhang, B. & Sadiq, M. (2020) Heterogeneous photodegradation of industrial dyes: An insight to different mechanisms and rate affecting parameters, *Journal of Environmental Chemical Engineering.* **8**, 104364.
23. Nguyen, L. T., Nguyen, H. T., Nguyen, L. T., Duong, A. T., Nguyen, H. Q., Ngo, V. T., Vu, N. V., Nguyen, D. T. C. & Van Tran, T. (2023) Efficient and recyclable Nd 3+-doped CoFe 2 O 4 for boosted visible-light-driven photocatalytic degradation of Rhodamine B dye, *RSC advances.* **13**, 10650-10656.
24. Sanadi, K., Rathod, K., Gaur, M., Powar, R., Parallel, V., Patil, R., Burungale, S. & Mali, A. (2021) UV light-activated photocatalytic degradation of rhodamine B dye and Suzuki cross-coupling reaction by Ni ferrite catalyst synthesizedsol–gel auto-combustion method, *Bulletin of Materials Science.* **44**, 1-8.
25. Das, K. C., Dhar, S. S., Thakurata, D. G. & Das, J. (2021) Sn (II) inserted on hydroxyapatite encapsulated nickel ferrite (NiFe2O4@ HAp-Sn2+): A novel nanocomposite for the effective photo-degradation of rhodamine B dye, *Journal of Cleaner Production.* **290**, 125172.
26. Jadhav, S. A., Khedkar, M. V., Andhare, D. D., Gopale, S. & Jadhav, K. (2021) Visible light photocatalytic activity of magnetically diluted Ni–Zn spinel ferrite for active degradation of rhodamine B, *Ceramics International.* **47**, 13980-13993.
27. Shakil, M., Inayat, U., Ashraf, M., Tanveer, M., Gillani, S. & Dahshan, A. (2023) Photocatalytic performance of novel zinc ferrite/copper sulfide composites for the degradation of Rhodamine B dye from wastewater using visible spectrum, *Optik.* **272**, 170353.
28. Nadeem, N., Zahid, M., Tabasum, A., Mansha, A., Jilani, A., Bhatti, I. A. & Bhatti, H. N. (2020) Degradation of reactive dye using heterogeneous photo-Fenton catalysts: ZnFe2O4 and GO-ZnFe2O4 composite, *Materials Research Express.* **7**, 015519.
29. Manohar, A., Chintagumpala, K. & Kim, K. H. (2021) Magnetic hyperthermia and photocatalytic degradation of rhodamine B dye using Zn-doped spinel Fe 3 O 4 nanoparticles, *Journal of Materials Science: Materials in Electronics.* **32**, 8778-8787.

Figures

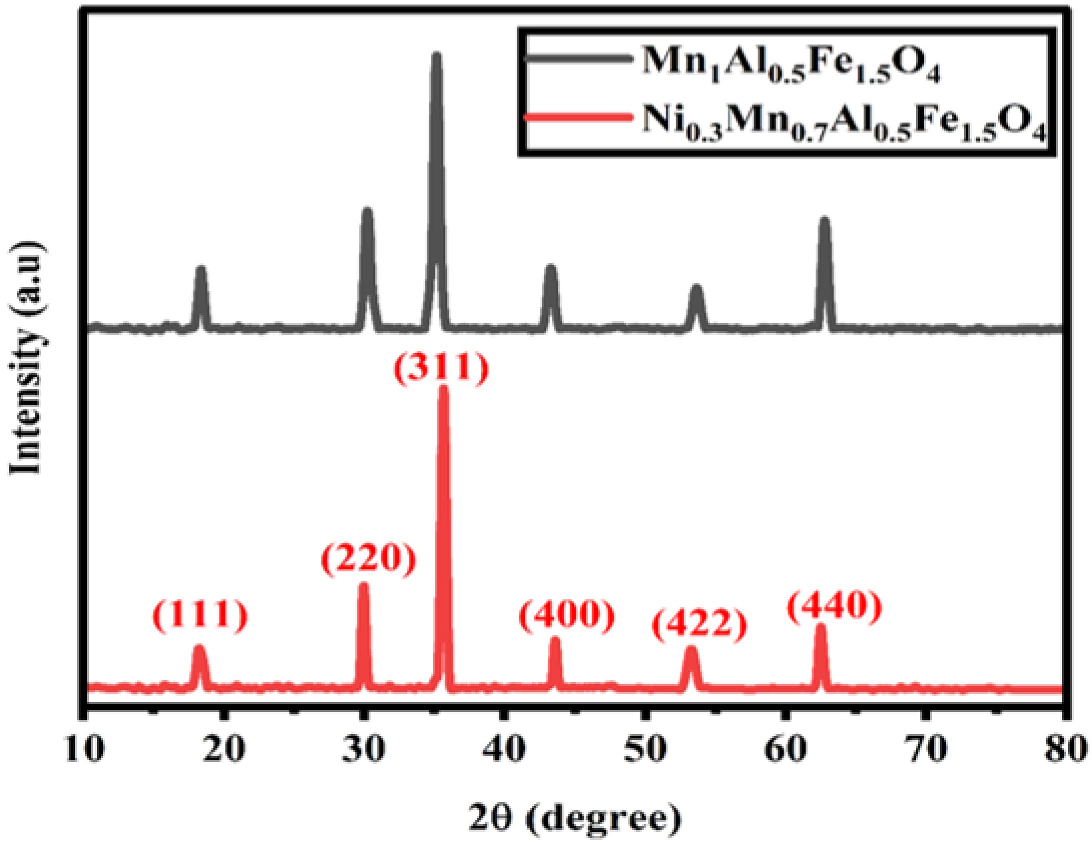

Figure 1

XRD graph of $Ni_XMn_{1-X}Al_{0.5}Fe_{1.5}O_4$ (X= 0,0.3)

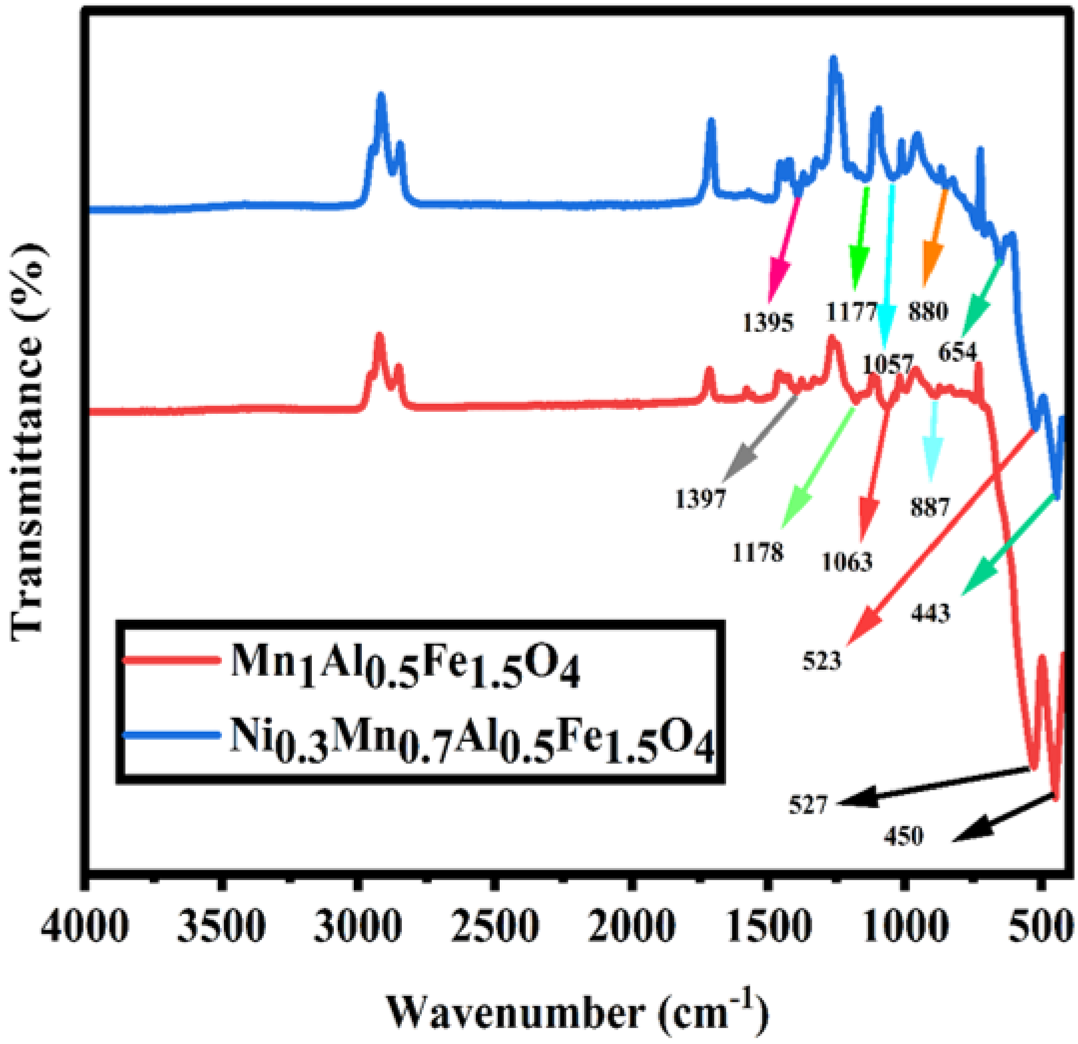

Figure 2

FTIR Analysis spectrum of $Ni_XMn_{1-X}Al_{0.5}Fe_{1.5}O_4$ (X= 0,0.3)

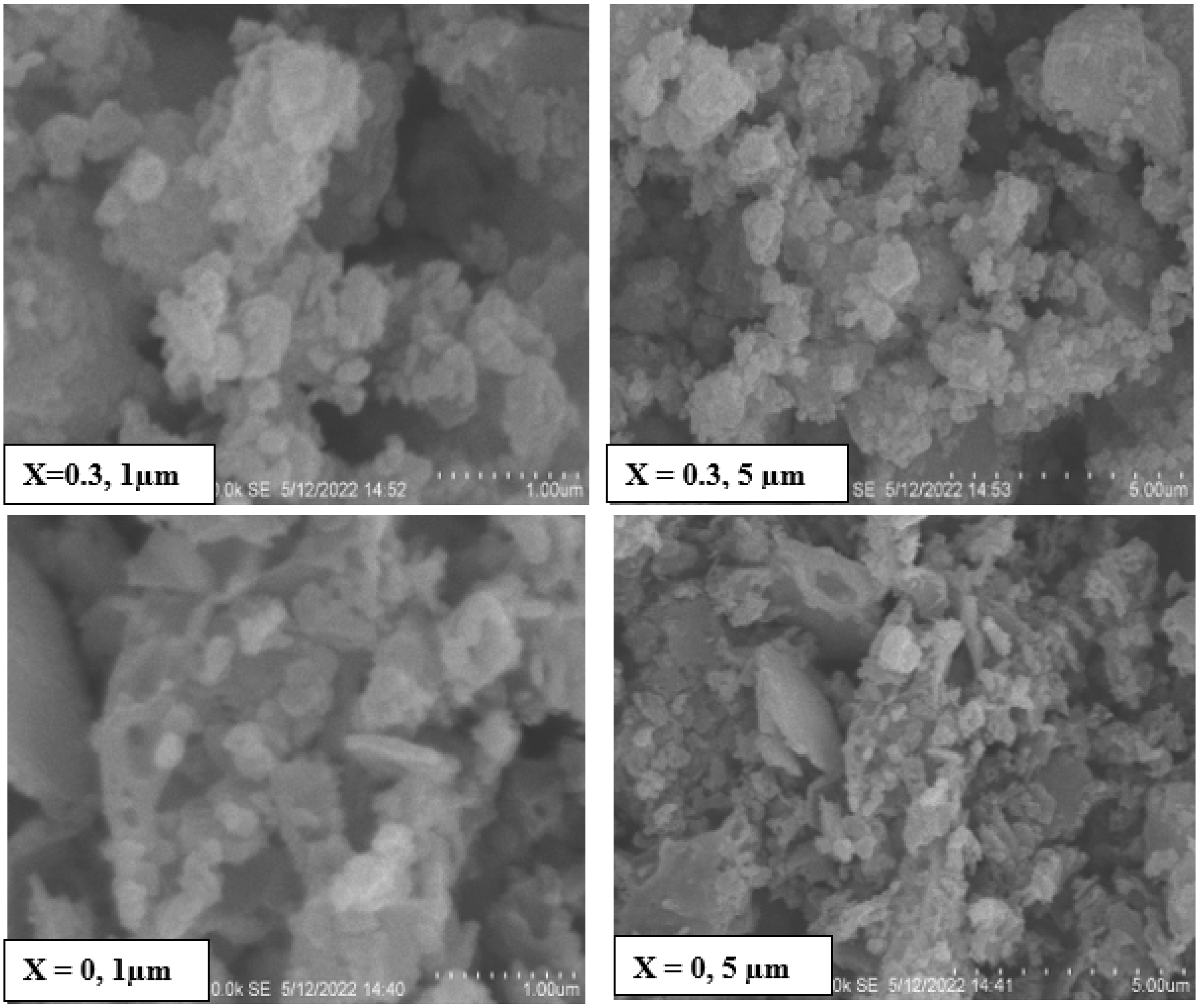

Figure 3

Sem Micrograph of $Ni_XMn_{1-X}Al_{0.5}Fe_{1.5}O_4$ (X = 0,0.3)

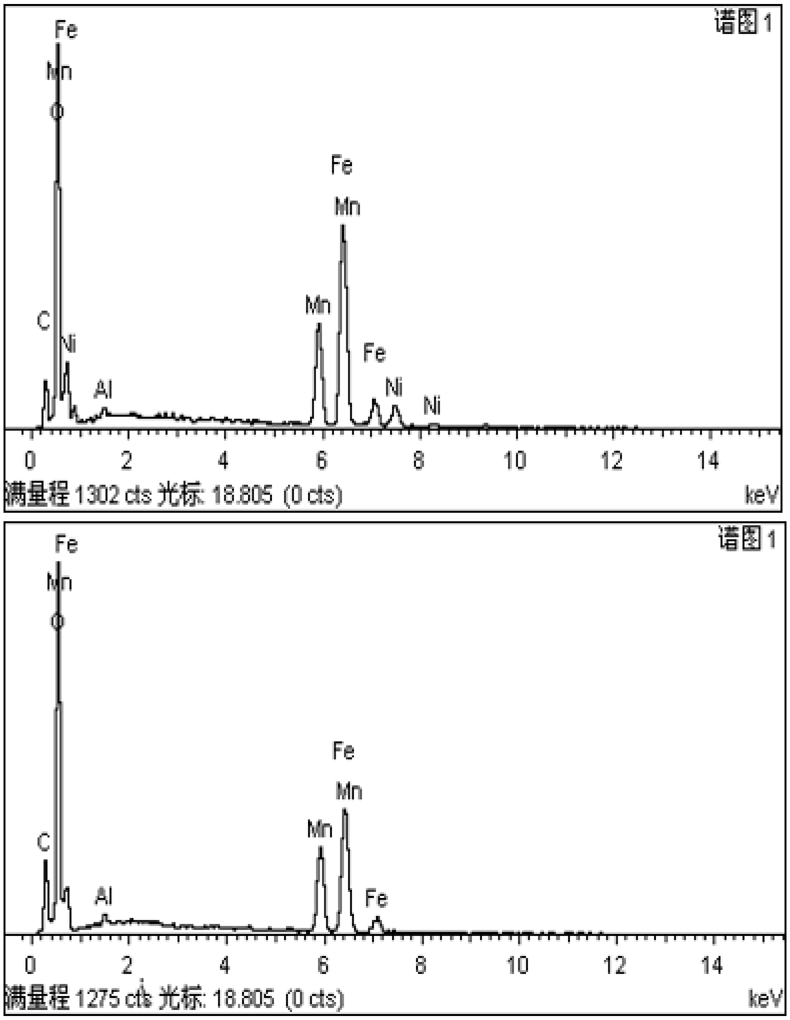

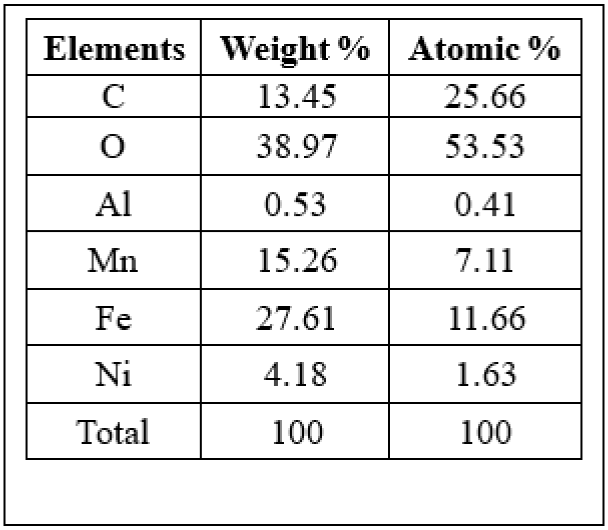

Elements	Weight %	Atomic %
C	13.45	25.66
O	38.97	53.53
Al	0.53	0.41
Mn	15.26	7.11
Fe	27.61	11.66
Ni	4.18	1.63
Total	100	100

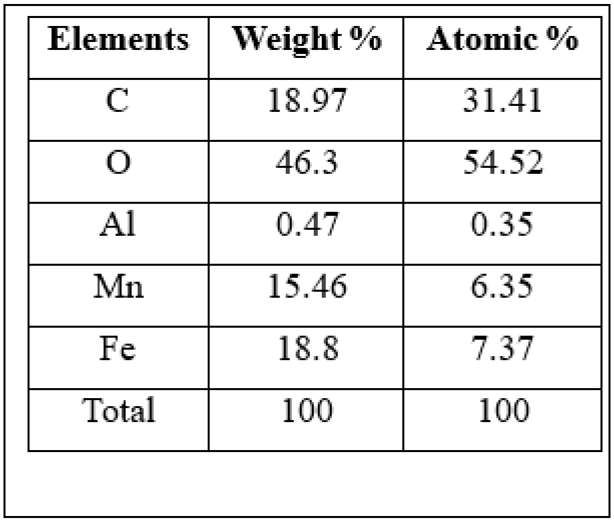

Elements	Weight %	Atomic %
C	18.97	31.41
O	46.3	54.52
Al	0.47	0.35
Mn	15.46	6.35
Fe	18.8	7.37
Total	100	100

Figure 4

EDX graphs and elemental composition of $Ni_XMn_{1-X}Al_{0.5}Fe_{1.5}O_4$ (X= 0,0.3)

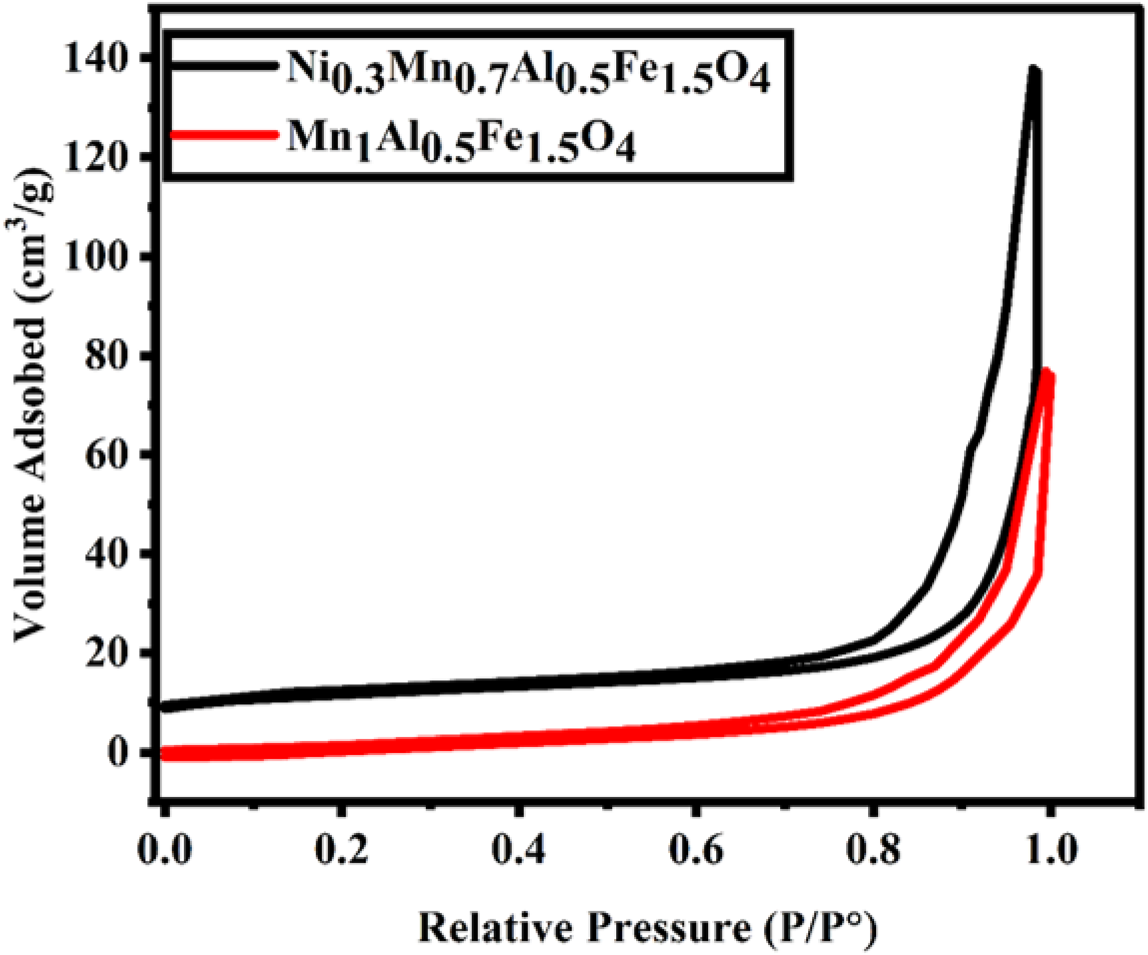

Figure 5

BET analysis of $Ni_XMn_{1-X}Al_{0.5}Fe_{1.5}O_4$ (X= 0,0.3)

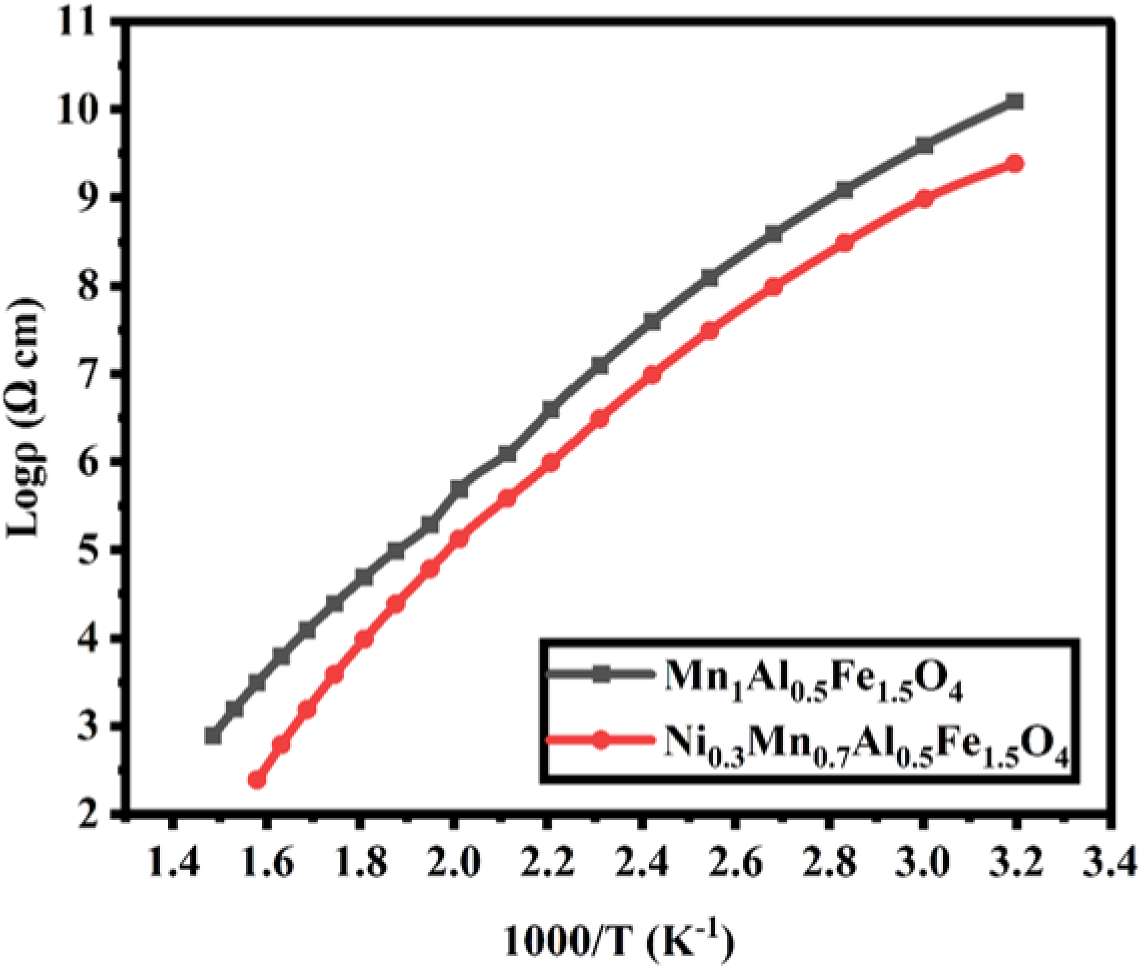

Figure 6

electrical resistivity of $Ni_XMn_{1-X}Al_{0.5}Fe_{1.5}O_4$ (X= 0,0.3)

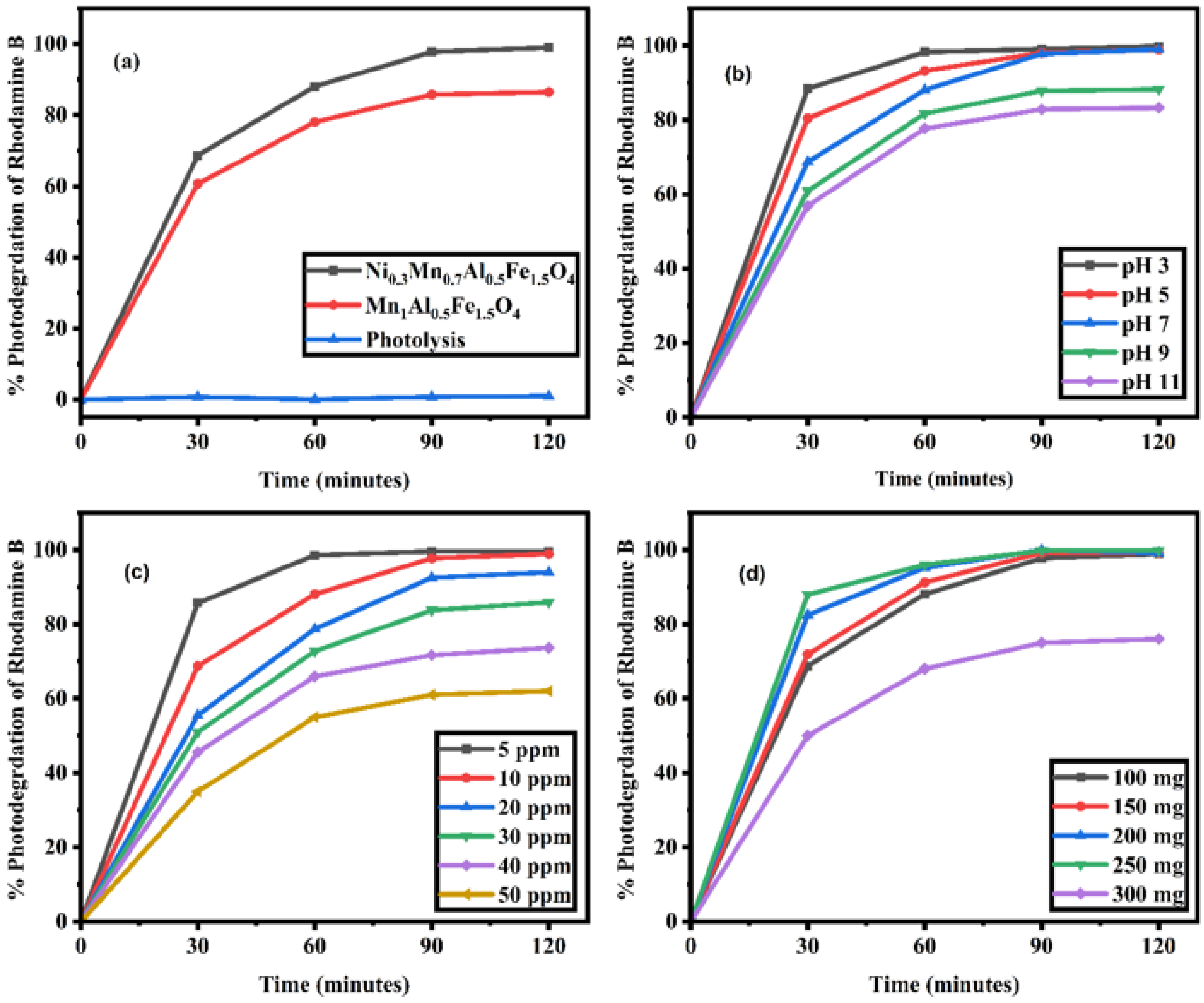

Figure 7

Influence of different factors on the removal of Congo red by $Ni_XMn_{1-X}Al_{0.5}Fe_{1.5}O_4$ ferrite. (a) effect of doping (b) effect of pH (c) dye concentration (d) catalyst dose, Normal Conditions [pH 7, Dye concentration 10 ppm, Catalyst dose 100 mg, Temperature 20°C, Light intensity 100 W except that factor which effect determine]

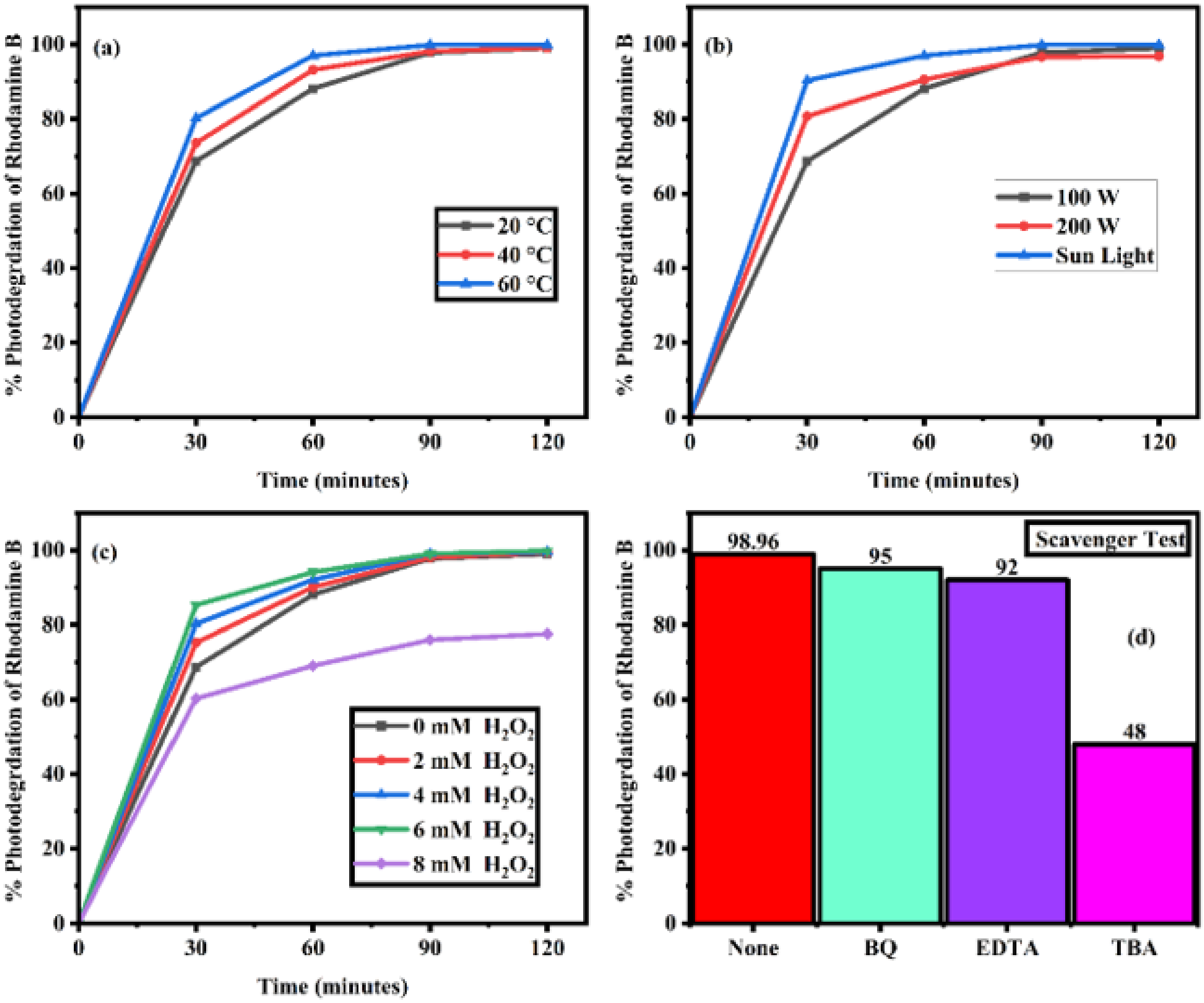

Figure 8

Removal efficiency of $Ni_XMn_{1-X}Al_{0.5}Fe_{1.5}O_4$ ferrite for rhodamine b under different conditions. (a) Temperature effect (b) effect of light Intensity (c) H_2O_2 Addition effect (d) Scavenger Analysis, Normal Conditions [pH 7, Dye concentration 10 ppm, Catalyst dose 100 mg, Temperature 20°C, Light intensity 100 W except that factor which effect determine]

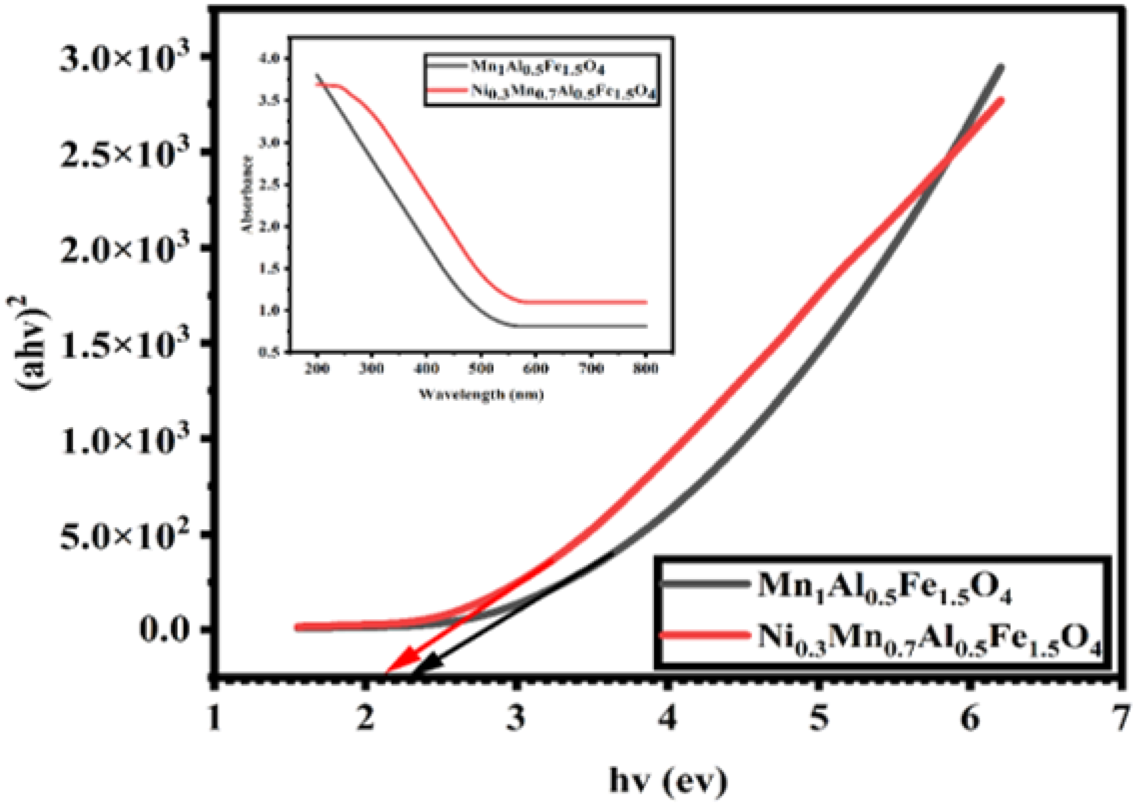

Figure 9

The UV-Visible DRS Spectra and Talc Graphs of $Ni_XMn_{1-X}Al_{0.5}Fe_{1.5}O_4$ (X= 0,0.3) ferrite.

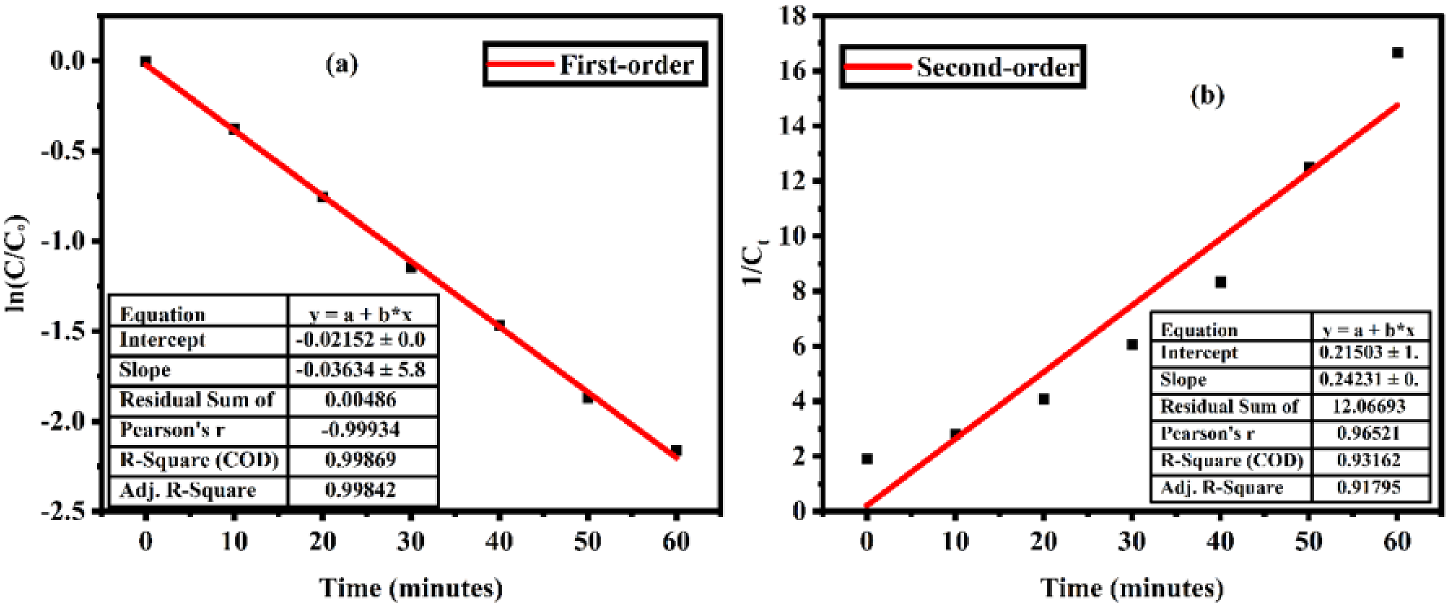

Equation	y = a + b*x
Intercept	-0.02152 ± 0.0
Slope	-0.03634 ± 5.8
Residual Sum of	0.00486
Pearson's r	-0.99934
R-Square (COD)	0.99869
Adj. R-Square	0.99842

Equation	y = a + b*x
Intercept	0.21503 ± 1.
Slope	0.24231 ± 0.
Residual Sum of	12.06693
Pearson's r	0.96521
R-Square (COD)	0.93162
Adj. R-Square	0.91795

Figure 10

kinetics model fitting (a)First order (b)Second order

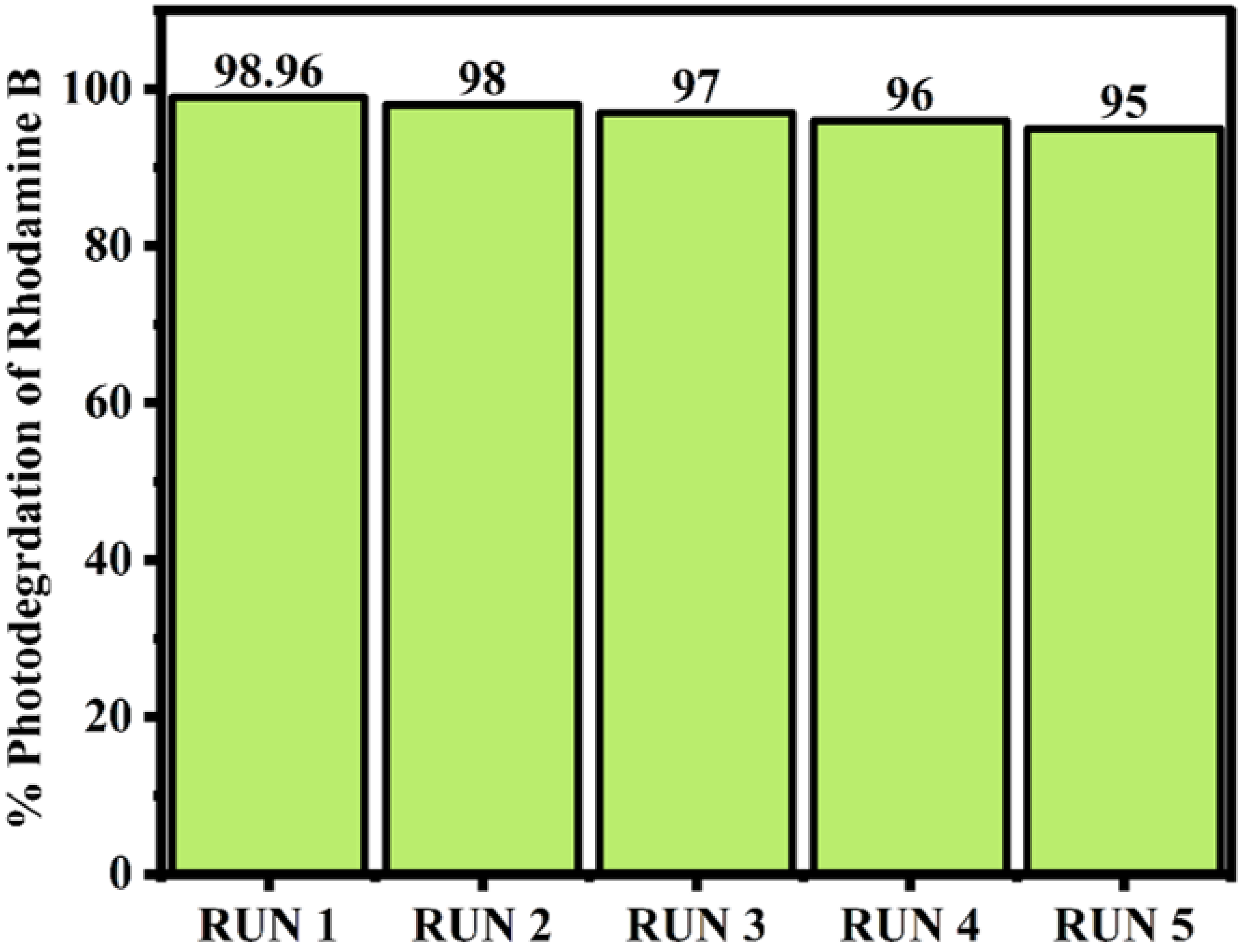

Figure 11

Recyclability of nickel-doped manganese aluminum ferrite